# Internal electric field engineering of bifunctional 2D/2D heterojunction photocatalyst for cooperative $H_2$ production and alcohol conversion

Guping Zhang, Shuting Huang, Xunxun Li, Dongyun Chen [*], Najun Li, Qingfeng Xu, Hua Li, Jianmei Lu [*]

*College of Chemistry, Chemical Engineering and Materials Science, Collaborative Innovation Center of Suzhou Nano Science and Technology, Soochow University, Suzhou, Jiangsu 215123, China*

## ARTICLE INFO

## ABSTRACT

Cooperative integrating of photocatalytic hydrogen ($H_2$) production and alcohol conversion is a prospective strategy for producing value-added fuels and chemicals to address the energy-related environmental issues. Herein, a bifunctional two-dimensional (2D)/2D $ZnIn_2S_4/CeO_2$ photocatalyst with a step-scheme heterojunction is successfully synthesized for simultaneous utilization of photogenerated electron-hole pairs, efficiently realizing the $H_2$ production coupled with furfuryl alcohol oxidative conversion in one photoredox reaction system. The optimized $ZnIn_2S_4/CeO_2$ photocatalyst produces 1.34 mmol $g^{-1}$ $h^{-1}$ of $H_2$ and 1.24 mmol $g^{-1}$ $h^{-1}$ of furfural, which is higher than pure $CeO_2$ and $ZnIn_2S_4$. The characterization results combined with density functional theory calculations revealed that the synergistic effect of 2D/2D heterointerfaces and internal electric field is importance for providing rich active sites and improving interfacial charge separation/transfer efficiency, therefore remarkably enhancing the photocatalytic redox performance. This study offers a paradigm for the future design of bifunctional photocatalysts for simultaneous $H_2$ production and alcohol conversion.

## 1. Introduction

Green and eco-sustainable solar energy can provide an unparalleled abundance of energy on Earth [1,2]. Photocatalytic $H_2$ production through water splitting is an important way to achieve solar-to-chemical-energy conversion [3–5]. Indium zinc sulfide ($ZnIn_2S_4$) is a nontoxic n-type reduction photocatalyst with visible light response, and has a sufficiently negative conduction band potential to enable a strong capacity for photogenerated electrons for reducing water [6,7]. However, pure $ZnIn_2S_4$ suffers from low photocatalytic performance because of inefficient separation and transfer of the photogenerated carriers [8–10]. Besides, most $ZnIn_2S_4$ catalysts have been synthesized using hydro/solvothermal approaches that result in self-assembly and stacking of 2D $ZnIn_2S_4$ nanosheets [11–13]. This aggregation greatly decreases the number of active sites in contact with water molecules, thus severely limiting photocatalytic $H_2$-production performance [14,15]. An effective strategy to overcome these problems is to fabricate specific structures of $ZnIn_2S_4$-based heterojunction photocatalysts.

Recently, a step-scheme (S-scheme) heterojunction, which consists of both reduction and oxidation photocatalysts, can facilitate interfacial charge transfer through an internal electric field and meanwhile realize maximized redox ability [16–18]. Cerium oxide ($CeO_2$) is an n-type oxidation photocatalyst with a quite positive valence band, high chemical stability, and unique electronic characteristics. It has been preferentially used as a support or composite material to improve photocatalytic activity [19,20]. The growth of 2D $ZnIn_2S_4$ nanosheets on 2D substrates has proved to be a highly effective modification strategy that not only inhibits aggregation and exposes abundant catalytic reactive sites, but also obtains the advantage of shortened charge transport distances from 2D/2D heterostructures [14,21–23]. Therefore, an establishment of 2D/2D S-scheme $ZnIn_2S_4/CeO_2$ heterojunction is expected to simultaneously address the double problems of aggregation and high photogenerated carrier recombination rate of $ZnIn_2S_4$ photocatalyst.

Sacrificial reagents, such as lactic acid [24,25], $Na_2S/Na_2SO_3$ [26], triethanolamine (TEOA) [27–29], and methanol [30], have been usually used in photocatalytic $H_2$ production reactions to accelerate water-oxidation half-reaction kinetics and restrain rapid charge recombination. However, this increases costs, wastes the oxidation capabilities of the photogenerated holes, and creates difficulties for
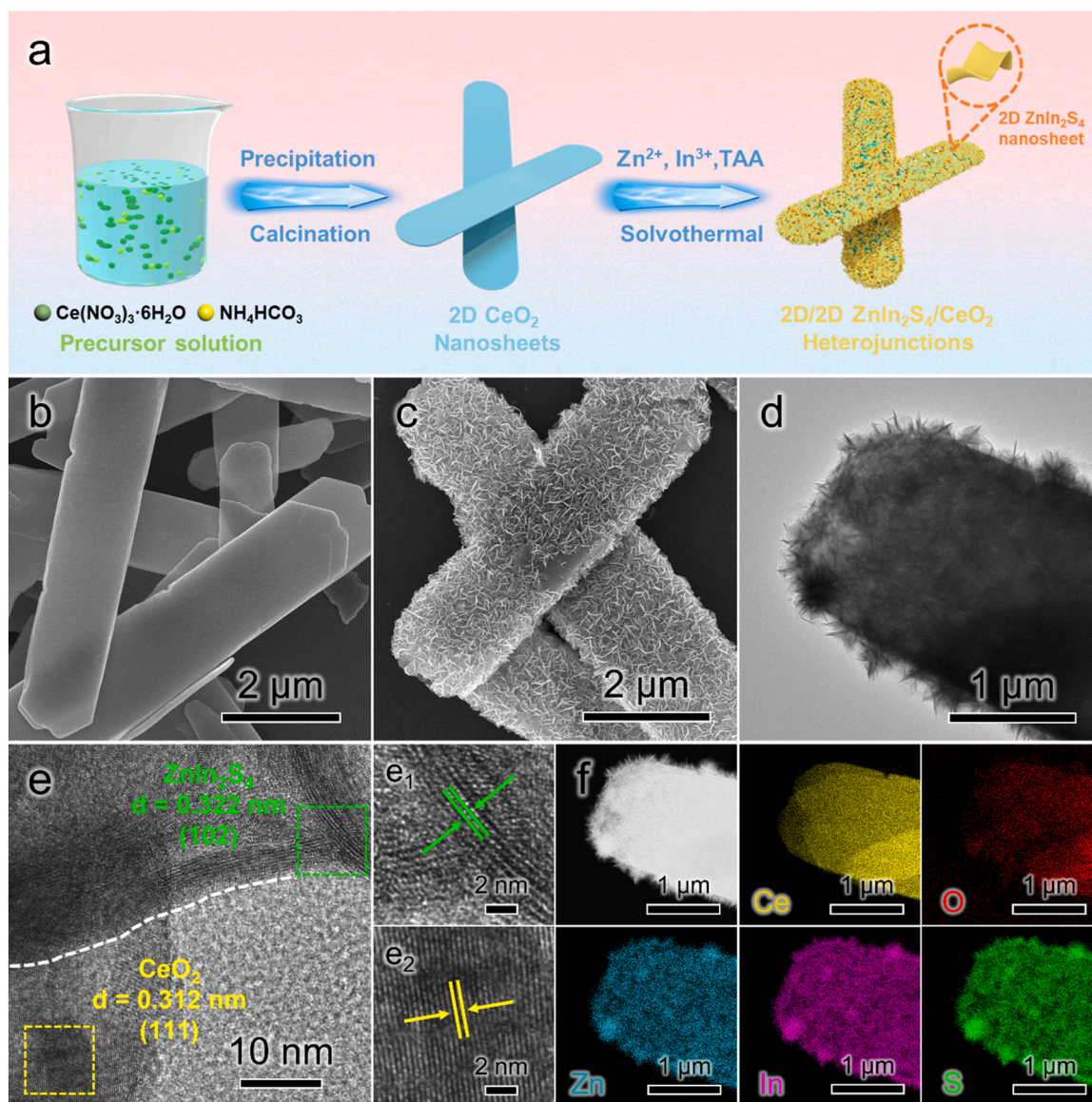
**Fig. 1.** (a) Schematic illustration of the fabrication of 2D/2D ZnIn$_2$S$_4$/CeO$_2$ heterojunction photocatalyst. (b) SEM image of CeO$_2$ nanosheets. (c) SEM, (d) TEM, and (e) HRTEM images of prepared ZnIn$_2$S$_4$/CeO$_2$-0.8 heterojunctions. (f) HAADF-STEM image and corresponding EDX elemental mappings of Ce, O, Zn, In, and S elements in ZIS/CeO$_2$-0.8 heterojunctions.

mechanistic studies. Hence, organic oxidation reactions have been introduced to replace hole scavengers for realizing the value-added hole utilization [31,32]. Solar-driven conversion of biomass-derived alcohols such as benzyl alcohol [33–35], furfuryl alcohol (FOL) [36,37], and cinnamyl alcohol [38] into high-value chemical products has drawn substantial interest. Furfural (FAL) is widely used as an important raw material for the synthesis of coatings, rubber, and pharmaceuticals, and can be produced via photocatalytic oxidation of FOL [39–41]. Therefore, the integration of photocatalytic H$_2$ production with FOL oxidation in one reaction system would avoid the use of hole scavengers, and produce clean H$_2$ and value-added chemicals by simultaneously utilizing photogenerated electron-hole pairs. To date, an in-depth investigation of this photocatalytic redox activity and cooperative mechanism in 2D/2D ZnIn$_2$S$_4$/CeO$_2$ heterojunctions has not been reported.

In this work, a 2D/2D S-scheme heterojunction photocatalyst involving ZnIn$_2$S$_4$ nanosheets anchored on CeO$_2$ nanosheets was fabricated by using a facile in-situ solvothermal method. The S-scheme charge transfer pathway and a robust internal electric field over the ZnIn$_2$S$_4$/CeO$_2$ heterojunction can not only effectively inhibit useful

photogenerated electrons and holes from complexing, but also afford the photocatalyst with stronger redox capability. Apart from the heterojunction construction, the face-to-face 2D/2D structure can provide sufficient reactive sites and shorten the distance for charge transport. Consequently, the optimized ZnIn$_2$S$_4$/CeO$_2$ heterojunctions can simultaneously make use of electrons and holes for H$_2$ production coupled with FOL conversion, and display the higher photocatalytic redox performance compared with a single component. Finally, various characterization analyses and theoretical calculations were employed to thoroughly discuss the reasons for the enhanced performance of photocatalytic redox cooperative reaction.

## 2. Experimental section

### 2.1. Synthesis of CeO$_2$ nanosheets

Pure CeO$_2$ nanosheets were synthesized through a rapid precipitation and calcination method described in the literature [42]. In a typical procedure, 2.78 g of Ce(NO$_3$)$_3$·6 H$_2$O and 1.50 g of NH$_4$HCO$_3$ were
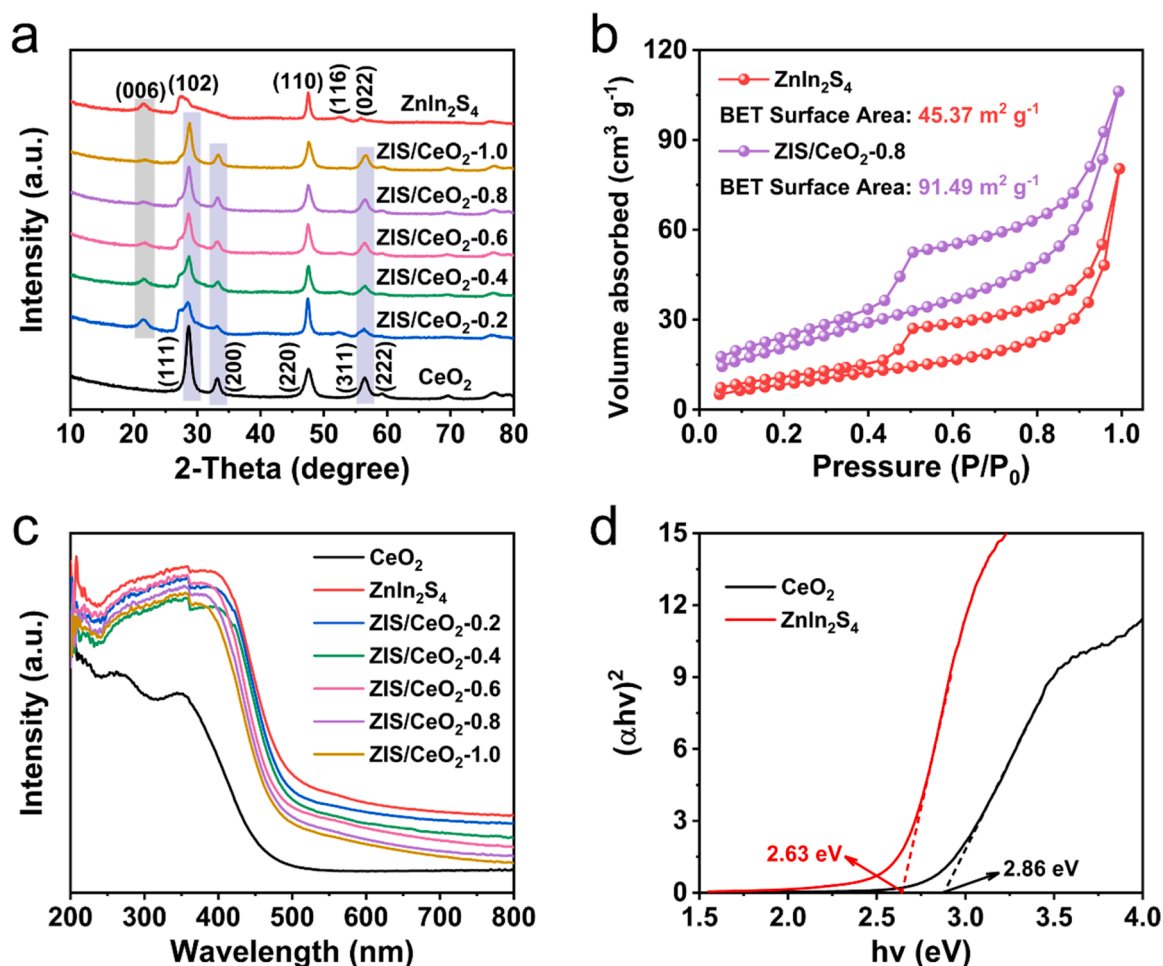
**Fig. 2.** (a) XRD patterns of the as-prepared $CeO_2$, $ZnIn_2S_4$, and $ZnIn_2S_4/CeO_2$ photocatalysts. (b) $N_2$ adsorption-desorption isotherms of $ZnIn_2S_4$ and ZIS/$CeO_2$-0.8 heterojunctions. (c) UV-Vis diffuse reflectance spectra of $CeO_2$, $ZnIn_2S_4$, and $ZnIn_2S_4/CeO_2$ photocatalysts. (d) Tauc plots of $CeO_2$ and $ZnIn_2S_4$ samples.

completely dissolved in 100 mL of ultrapure water under magnetic stirring condition, respectively. After that, the $NH_4HCO_3$ aqueous solution was quickly poured into the $Ce(NO_3)_3$ solution, continuously stirred for 0.5 h, and subsequently statically aged at 30 °C for 24 h. The formed precipitate was gathered by centrifugation, washed with ultrapure water and ethanol for several times, and dried under vacuum at 60 °C overnight. Finally, the collected white powder was thermally treated in air at 500 °C for 4 h with a heating rate of 2 °C min$^{-1}$ and then cooled to room temperature naturally, the $CeO_2$ nanosheets were obtained for further characterization and use.

### 2.2. Synthesis of 2D/2D $ZnIn_2S_4/CeO_2$ heterojunctions

A facile and efficient low-temperature solvothermal method was used to synthesize 2D/2D $ZnIn_2S_4/CeO_2$ heterojunctions [43,44]. Firstly, 32 mL of ultrapure water (pH = 2.5, adjusted by 0.5 mol L$^{-1}$ HCl) and 8 mL of glycerol were added into a round-bottom flask and stirred to form a homogeneous solution. Then, 1 mmol of $ZnCl_2$, 2 mmol of $InCl_3\cdot4$ $H_2O$ and 4 mmol thioacetamide (TAA) were dissolved in the above solution, followed by addition of certain amounts of $CeO_2$ nanosheets (e.g., 0.2, 0.4, 0.6, 0.8 and 1.0 mmol, respectively). The resulting mixture was stirred for 10 min and subsequently heated at 80 °C for 2 h in an oil bath under magnetic stirring. After cooling to room temperature, the solid products were centrifuged, washed several times with ultrapure water and ethanol, and finally dried overnight in vacuum at 60 °C. The synthesized products are labeled as ZIS/$CeO_2$-0.2, ZIS/$CeO_2$-0.4, ZIS/-$CeO_2$-0.6, ZIS/$CeO_2$-0.8 and ZIS/$CeO_2$-1.0, respectively. For

comparison, the pure flower-like $ZnIn_2S_4$ microspheres were synthesized under the same reaction conditions without the addition of 2D $CeO_2$ nanosheets.

### 2.3. Photocatalytic performance testing

The cooperative experiments of photocatalytic $H_2$ production and FOL conversion were implemented in a sealed online automatic detection system (Labsolar-6A, Beijing Perfectlight). Typically, 10 mg of powder samples were scattered in 100 mL of a mixed aqueous solution containing 10 mL of FOL and then sonicated for 0.5 h to ensure homogeneity. The temperature of the reaction system was maintained at 10 °C through circulating cooling water, and the light source was a 300 W Xenon lamp (PLS-SXE 300D, Beijing Perfectlight) equipped with a 400 nm cutoff filter. Before irradiation, the reaction system was vacuumed for 0.5 h to completely remove the air and dissolved oxygen. With continuous light irradiation for 5 h, the produced $H_2$ was collected at the given time intervals and quantitatively analyzed by a gas chromatography (GC, FL9790II) equipped with a 5 A molecular sieve columns, a thermal conductivity detector (TCD), and with Ar as the carrier gas. Meanwhile, the yields of liquid products were detected by a high-performance liquid chromatography (HPLC, Agilent 1260 Infinity II). Besides, the consumption ratio of electrons and holes [R(e$^-$/h$^+$)] in this photoredox synergistic reaction was calculated by using the following formula (1):
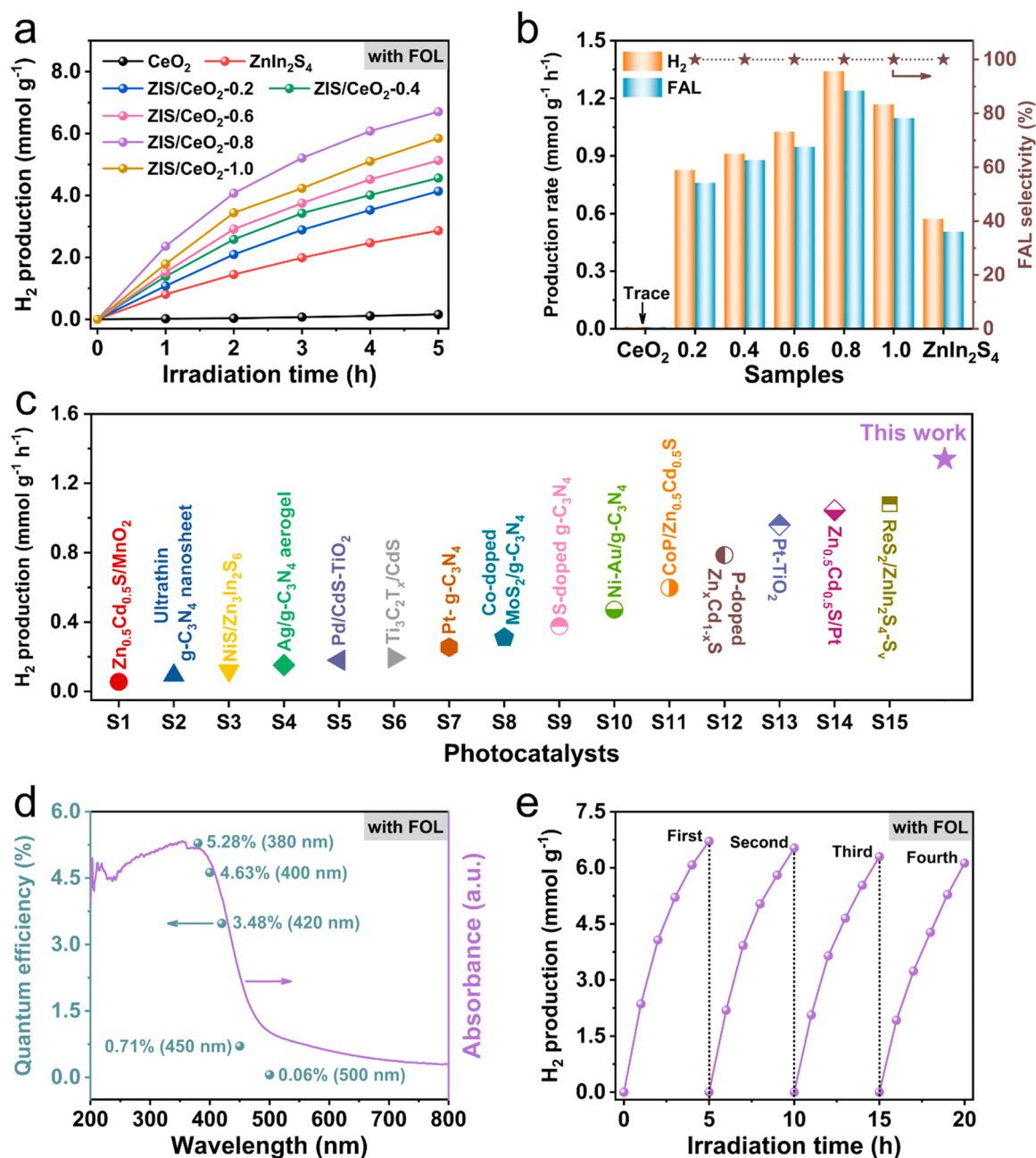
$$R(e^-/h^+) = \frac{n_{H_2}}{n_{FAL}} \quad (1)$$

**Fig. 3.** (a) Time-dependent photocatalytic $H_2$ production curves of different samples in the aqueous solution of FOL. (b) The corresponding $H_2$ and FAL production rates over different samples. (c) Comparison of photocatalytic $H_2$ production performance with some reported photocatalysts in the cooperative photoredox reaction systems. (d) Wavelength dependence quantum efficiency of ZIS/CeO$_2$-0.8 heterojunctions under different monochromatic lights. (e) Photocatalytic cyclic experiments of $H_2$ production over ZIS/CeO$_2$-0.8 heterojunctions.

where $n_{H_2}$ and $n_{FAL}$ are the moles of $H_2$ and FAL products, respectively. The apparent quantum efficiency (AQE) measurement was performed under monochromatic light irradiation with the bandpass filters of 380, 400, 420, 450 and 500 nm, respectively. The AQE value was calculated by using the following formula (2):

$$\begin{aligned} AQE &= \frac{\text{number of reacted electrons}}{\text{number of incident photons}} \times 100\% \\ &= \frac{\text{number of evolved } H_2 \text{ molecules} \times 2}{\text{number of incident photons}} \times 100\% \end{aligned} \quad (2)$$

## 3. Results and discussion

### 3.1. Characterization of $ZnIn_2S_4/CeO_2$ heterojunction

The fabrication routes of 2D/2D $ZnIn_2S_4/CeO_2$ heterojunction photocatalysts are displayed schematically in Fig. 1a. The 2D CeO$_2$ nanosheets were synthesized via a rapid precipitation and calcination. Then, ultrathin 2D $ZnIn_2S_4$ nanosheets were anchored on the CeO$_2$ nanosheets in an efficient low-temperature solvothermal process to construct $ZnIn_2S_4/CeO_2$ heterojunctions with unique 2D/2D structures.

The morphologies of as-prepared photocatalysts were first observed by the scanning electron microscopy (SEM) and transmission electron microscopy (TEM). As demonstrated in Fig. 1b and S1 (Supporting Information), pristine CeO$_2$ samples possess regular belt-like sheet

structure with a width of approximately 1–2 μm and a length of 5–10 μm. The atomic force microscopy (AFM) height profiles reveal the thickness of the $CeO_2$ nanosheets are about 16 nm (Fig. S2), which is basically in accordance with the previous study [42]. Fig. S3 depicts the successful fabrication of flower-like $ZnIn_2S_4$ microspheres self-assembled from numerous nanosheets. Interestingly, Fig. 1c,d show that the constructed $ZnIn_2S_4/CeO_2$ heterojunctions possess beautiful 2D/2D structures, where the small $ZnIn_2S_4$ nanosheets intercross with each other and uniformly grow on the larger $CeO_2$ nanosheets, forming reliable and intimate contact interfaces. In Fig. 1e, a high-resolution TEM (HRTEM) image reveals that two sets of lattice fringes with spacings of 0.312 and 0.322 nm, which are attributed to the (111) and (102) crystal planes of $CeO_2$ and $ZnIn_2S_4$, respectively [45,46]. The energy-dispersive X-ray spectra (EDX) spectrum (Fig. S4) confirms that the constituent elements of ZIS/$CeO_2$-0.8 heterojunctions are Ce, O, Zn, In, and S. High-angle annular dark-field TEM (HAADF-TEM) and elemental mapping images (Fig. 1f) further clearly suggest that $ZnIn_2S_4$ nanosheets are well distributed on the $CeO_2$ nanosheets, reaffirming the formation of 2D/2D heterostructures of $ZnIn_2S_4/CeO_2$ photocatalysts. Furthermore, the specific surface areas and pore sizes distribution of catalysts were determined by Brunauer-Emmett-Teller (BET) technology. From Fig. 2b and S5, the $ZnIn_2S_4/CeO_2$-0.8 heterojunctions have increased specific surface areas of 91.49 $m^2 g^{-1}$ relative to those of $CeO_2$ (60.61 $m^2 g^{-1}$) and $ZnIn_2S_4$ (45.37 $m^2 g^{-1}$). A significant H3-type hysteresis loop in the type-IV isotherm of $ZnIn_2S_4/CeO_2$-0.8 heterojunctions and corresponding pore size distribution curve (Fig. S6) indicate the presence of narrow slit-shaped nanopores deriving from randomly distributed 2D $ZnIn_2S_4$ nanosheets [7]. Overall, these results evidence that the $ZnIn_2S_4/CeO_2$ heterojunction photocatalysts have well-formed 2D/2D structures, with tight interface connections, high specific surface areas, and suitable mesoporous structures for interfacial charge transfer and mass transport of reactants and products.

The phase structures of the synthesized photocatalysts were then analyzed by X-ray powder diffraction (XRD), as shown in Fig. 2a. Pristine $CeO_2$ displays diffraction peaks at 28.6°, 33.1°, 47.5°, 56.3°, and 59.1°, which are individually indexed to the (111), (200), (220), (311), and (222) planes of cubic $CeO_2$ (JCPDS No. 34–0394) [42]. For pure $ZnIn_2S_4$, all the diffraction peaks are consistent with its hexagonal phase (JCPDS No. 65–2023) [44,46]. As expected, the diffraction peaks of $CeO_2$ and $ZnIn_2S_4$ are detected in the $ZnIn_2S_4/CeO_2$ heterojunctions, and no other miscellaneous peaks are observed. Furthermore, the diffraction peak intensity of $CeO_2$ in $ZnIn_2S_4/CeO_2$ heterojunctions gradually enhances with the increased content of $CeO_2$, while the diffraction peak intensity of $ZnIn_2S_4$ becomes weaker. These XRD results indicate that high-purity $ZnIn_2S_4/CeO_2$ heterojunctions are successfully constructed.

In addition, the optical absorption characteristics of catalysts were investigated using UV-Vis diffuse reflectance spectra (DRS) and corresponding results are shown in Fig. 2c. Pure $CeO_2$ has an absorption edge at around 460 nm, whereas $ZnIn_2S_4$ shows a stronger visible light absorption edge of 520 nm. According to Tauc plots, calculated band gap energies ($E_g$) for $CeO_2$ and $ZnIn_2S_4$ are 2.86 eV and 2.63 eV, respectively (Fig. 2d). Furthermore, all prepared $ZnIn_2S_4/CeO_2$ heterojunction photocatalysts exhibit excellent absorption capability of visible light, implying they can make full use of visible light to generate sufficient electron-hole pairs needed for the photocatalytic reactions.

### 3.2. Photocatalytic performance evaluation

As noted in the introduction, value-added utilization of photogenerated holes is an alternative to costly sacrificial agents for advancing the future application of photocatalytic $H_2$ production. Therefore, the photocatalytic performance of the prepared samples was evaluated in a redox dual-functional system integrated $H_2$ production with FOL oxidation conversion under visible light irradiation. As shown in Fig. 3a,b, pristine $CeO_2$ is inactive for photoredox reaction, and the nanosheets-assembled $ZnIn_2S_4$ exhibits low production rates for $H_2$

(0.57 mmol $g^{-1}$ $h^{-1}$) and FAL (0.51 mmol $g^{-1}$ $h^{-1}$). In contrast, with construction of heterojunction between $CeO_2$ and $ZnIn_2S_4$, the production rates of $H_2$ and FAL over $ZnIn_2S_4/CeO_2$ heterojunctions display significantly increasing trends. In particular, the ZIS/$CeO_2$-0.8 heterojunctions possess the best $H_2$ production rate of 1.34 mmol $g^{-1}$ $h^{-1}$, which is approximately 2.35 times higher than that of pure $ZnIn_2S_4$ and superior to some reported photocatalysts in cooperative photoredox reaction systems (Fig. 3c and Table S1, Supporting Information). Meanwhile, the corresponding highest FAL production rate approaches 1.24 mmol $g^{-1}$ $h^{-1}$, and no any other products except FAL are found in the liquid (Fig. S7), suggesting the ultra-high selectivity for FAL product. However, upon further increasing $CeO_2$ content, the photocatalytic performance of ZIS/$CeO_2$-1.0 heterojunctions decreases because overmuch $CeO_2$ may induce more recombination centers of photogenerated charges [47,48]. In Fig. S8, the same order of photocatalytic activity of synthesized samples is also observed when conventional TEOA is utilized as a scavenger, and the ZIS/$CeO_2$-0.8 heterojunctions afford a maximum $H_2$ production rate of 5.53 mmol $g^{-1}$ $h^{-1}$ (Fig. S9). Although using FOL is not as efficient as TEOA for photocatalytic $H_2$ production, it is meaningful for improving utilization of photogenerated holes to obtain high value-added FAL products. Furthermore, in this photoredox reaction system, it is found that the consumption ratio of electrons and holes [R(e$^-$/h$^+$)] is about 1.0 based on the co-production yield of $H_2$ and FAL, implying a stoichiometric dehydrogenation reaction [49].

Subsequently, a series of control experiments were performed to investigate the effects of experimental conditions on the photocatalytic performance over ZIS/$CeO_2$-0.8 heterojunctions. As displayed in Figs. S10 and S11, when the reaction is run in the absence of photocatalyst or under dark condition, no $H_2$ products are detected, revealing that the present reaction is undoubtedly driven by photocatalysis. In addition, the $H_2$ production rate obviously decreases to 0.24 mmol $g^{-1}$ $h^{-1}$ with ZIS/$CeO_2$-0.8 heterojunctions when using acetonitrile (MeCN) as a solvent to substitute water, and no $H_2$ is generated in pure MeCN solution, confirming that the produced $H_2$ mainly originates from water splitting while small amounts of hydrogen is derived from dehydrogenation of FOL. As illustrated in Fig. S12, the photocatalytic $H_2$ production performance of ZIS/$CeO_2$-0.8 heterojunctions is enhanced with increasing the concentration of FOL. This can be contributed to that a relatively high concentrations is beneficial to facilitate their mass transfer from bulk solution toward the photocatalyst surface, thereby improving their surface coverages and accelerating the oxidation reaction with holes to effectively inhibit the electron-hole recombination [50].

Furthermore, the AQE of optimized $ZnIn_2S_4/CeO_2$-0.8 heterojunctions was determined from the wavelength-dependent $H_2$ production efficiency. As observed in Fig. 3d, the AQE values of ZIS/$CeO_2$-0.8 severally reach 5.28% (380 nm), 4.63% (400 nm), 3.48% (420 nm), 0.71% (450 nm), and 0.06% (500 nm), which roughly maintain the variation trend of its optical absorption spectrum, meaning that the light excitation of ZIS/$CeO_2$-0.8 heterojunctions drive this photocatalytic reaction [51,52]. The stability of the ZIS/$CeO_2$-0.8 photocatalyst was also assessed by multiple cycle experiments, and the results are displayed in Fig. 3e and S13. Apparently, no significant activity loss is observed for $ZnIn_2S_4/CeO_2$-0.8 photocatalyst after four cycles, indicating its favorable stability. Moreover, as can be seen in Figs. S14 and S15, the phase structure and 2D/2D morphological structure of the recycled ZIS/$CeO_2$-0.8 are well kept compared to the initial sample, manifesting the stable chemical and structural properties of ZIS/-$CeO_2$-0.8 heterojunctions.

### 3.3. Mechanism of photocatalytic performance enhancement

To better understand the enhanced photocatalytic performance of synthesized $ZnIn_2S_4/CeO_2$ heterojunctions, photoelectrochemical characterizations were first performed to examine the behaviors (separation, transfer, and recombination) of photogenerated electron-hole pairs.
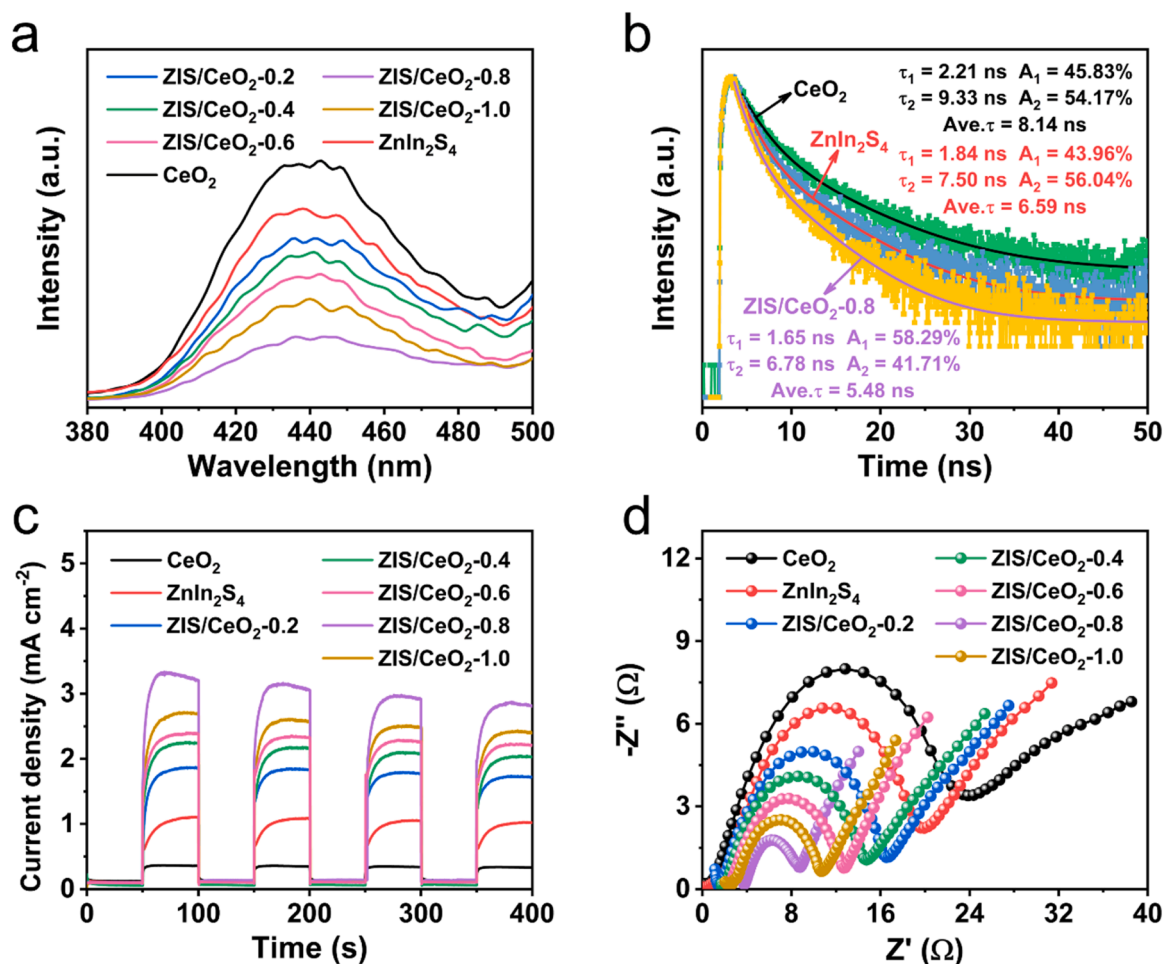
**Fig. 4.** (a) Steady-state PL spectra, (b) TRPL spectra, (c) transient photocurrent responses, and (d) EIS plots of the prepared of photocatalysts.

From the steady-state photoluminescence (PL) spectra in Fig. 4a, compared with pure $ZnIn_2S_4$ and $CeO_2$, all the $ZnIn_2S_4/CeO_2$ heterojunctions display weaker PL intensity, especially $ZIS/CeO_2$-0.8 sample has the weakest intensity, indicating the recombination of photogenerated electron-hole pairs is greatly restrainted [21,43]. Meanwhile, time-resolved photoluminescence (TRPL) spectra were acquired to characterize charge transfer dynamics (Fig. 4b). As is clearly seen, the average lifetime of $ZIS/CeO_2$-0.8 heterojunctions (5.48 ns) is much shorter than that of $ZnIn_2S_4$ (6.59 ns) and $CeO_2$ (8.14 ns). This reduced fluorescence lifetime indicates that there is a nonradiative path when electron transfer between $ZnIn_2S_4$ and $CeO_2$, and the photogenerated carriers separation and migration are accelerated [22,53,54].

In addition, the charge separation efficiency of the photocatalysts was verified by transient photocurrent response and electrochemical impedance spectroscopy (EIS) measurements. In Fig. 4c, the photocurrent densities of $ZnIn_2S_4/CeO_2$ heterojunctions are much higher than those of pure $CeO_2$ and $ZnIn_2S_4$, indicating efficient separation and transfer of photogenerated electrons and holes in $ZnIn_2S_4/CeO_2$ heterojunction photocatalysts [44,51,53]. Meanwhile, the EIS Nyquist plots of the prepared samples are presented in Fig. 4d to evaluate the resistance of interfacial charge transfer, where a smaller semicircle radius generally reflects a lower charge transfer resistance [30,46]. Obviously, the $ZIS/CeO_2$-0.8 heterojunctions have the smallest arc radius among all the synthesized samples, implying the lowest migration resistance for charge carriers. Therefore, all these results validate that the efficient separation and rapid transfer of photogenerated electrons and holes are significant factors for the enhancement of photocatalytic performance.

X-ray photoelectron spectroscopy (XPS) was then used to

characterize the chemical states of the component elements as well as electron transfer behavior. In Fig. S16, the XPS survey spectrum reveals the presence of Zn, In, S, Ce, and O in the $ZnIn_2S_4/CeO_2$-0.8 heterojunctions. As for pure $CeO_2$, the high-resolution XPS spectra of Ce 3d can be fitted into eight peaks, where v and u were assigned to Ce $3d_{5/2}$ and Ce $3d_{3/2}$, respectively (Fig. 5a) [55]. Specifically, three peaks at v (882.3 eV), v″ (888.6 eV) and v‴ (898.2 eV) are attributed to Ce $3d_{5/2}$, and other three peaks at u (900.7 eV), u″ (907.4 eV) and u‴ (916.6 eV) correspond to Ce $3d_{3/2}$ [56]. These six peaks mentioned above confirm the presence of $Ce^{4+}$, whereas the two peaks of v′ (884.6 eV) and u′ (903.2 eV) are belonged to $Ce^{3+}$ [55–57]. Fig. 5b presents the high-resolution O 1 s spectra, where the peaks located at 529.4 and 531.2 eV are corresponded to lattice oxygen and surface adsorbed oxygen in $CeO_2$, respectively [48]. For pristine $ZnIn_2S_4$, the peaks located at 1021.9 and 1044.9 eV are distributed to Zn $2p_{3/2}$ and Zn $2p_{1/2}$, respectively (Fig. 5c) [13], and the two peaks at 444.9 and 452.5 eV are ascribed to the $3d_{5/2}$ and $3d_{3/2}$ of In, respectively (Fig. 5d) [58]. Meanwhile, the peaks at 161.6 eV and 162.8 eV correspond to S $2p_{3/2}$ and S $2p_{1/2}$ in $ZnIn_2S_4$ [59], are observed in Fig. 5e. It is noteworthy that, the binding energies of Ce 3d and O 1 s of $ZIS/CeO_2$-0.8 heterojunctions become more negative in darkness with respect to those of pristine $CeO_2$, while the binding energies of Zn 2p, In 3d, and S 2p in $ZIS/CeO_2$-0.8 heterojunctions are more positively shifted in the dark compared with pure $ZnIn_2S_4$. These XPS binding energy shifts support the migration of electrons from $ZnIn_2S_4$ to $CeO_2$ upon contact between them, inducing the formation of an internal electric field at the interface along the direction from $ZnIn_2S_4$ to $CeO_2$ [7,59,60]. Furthermore, as depicted in Fig. 5f, the planar-averaged charge density difference (Δρ)
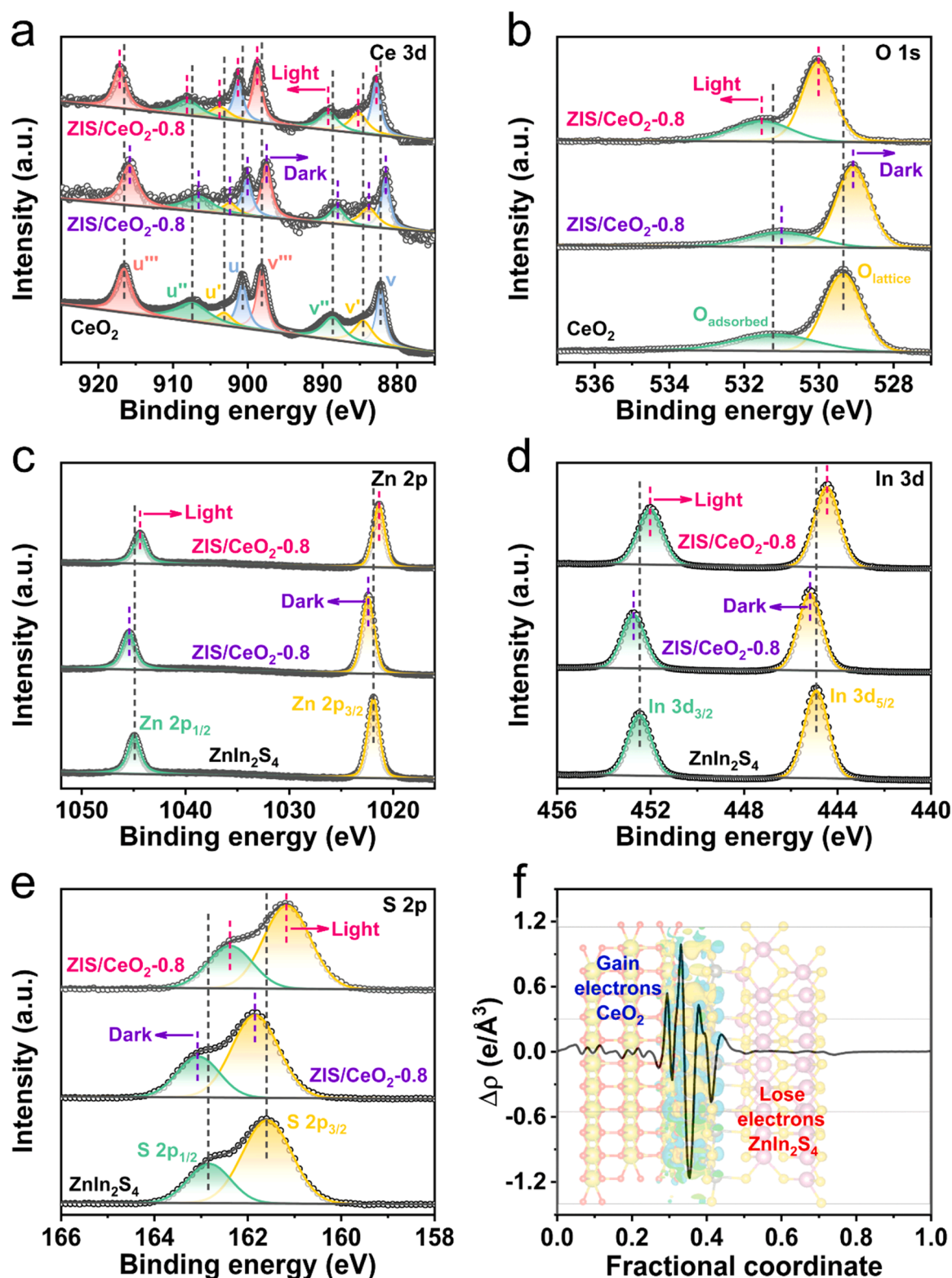
**Fig. 5.** High-resolution XPS spectra of (a) Ce 3d and (b) O 1 s from $CeO_2$ and $ZnIn_2S_4/CeO_2$-0.8 samples in darkness and under irradiation. High-resolution XPS spectra of (c) Zn 2p, (d) In 3d, and (e) S 2p of $ZnIn_2S_4$ and $ZnIn_2S_4/CeO_2$-0.8 samples in darkness and under irradiation. (f) The planar averaged charge density difference of $ZnIn_2S_4/CeO_2$ heterojunction (The insert represents the side view of the charge density difference over the $ZnIn_2S_4/CeO_2$ heterojunction).

evidently confirms a strong interaction at the interface of $CeO_2$ and $ZnIn_2S_4$ in $ZnIn_2S_4/CeO_2$ heterojunction, and the direction of electron transfer is consistent with the XPS analyses. Subsequently, when in-situ irradiated XPS was carried out, compared with ZIS/$CeO_2$-0.8 heterojunctions in the dark, the binding energies of Ce 3d and O 1 s in the

ZIS/$CeO_2$-0.8 heterojunctions under light irradiation are positively shifted (Fig. 5a,b) whereas the Zn 2p, In 3d, and S 2p display negative shifts (Fig. 5c-e), demonstrating the photogenerated electrons migrate from $CeO_2$ to $ZnIn_2S_4$. Hence, these XPS results provide significant bases of charge transfer directions for the $ZnIn_2S_4/CeO_2$ heterojunction upon
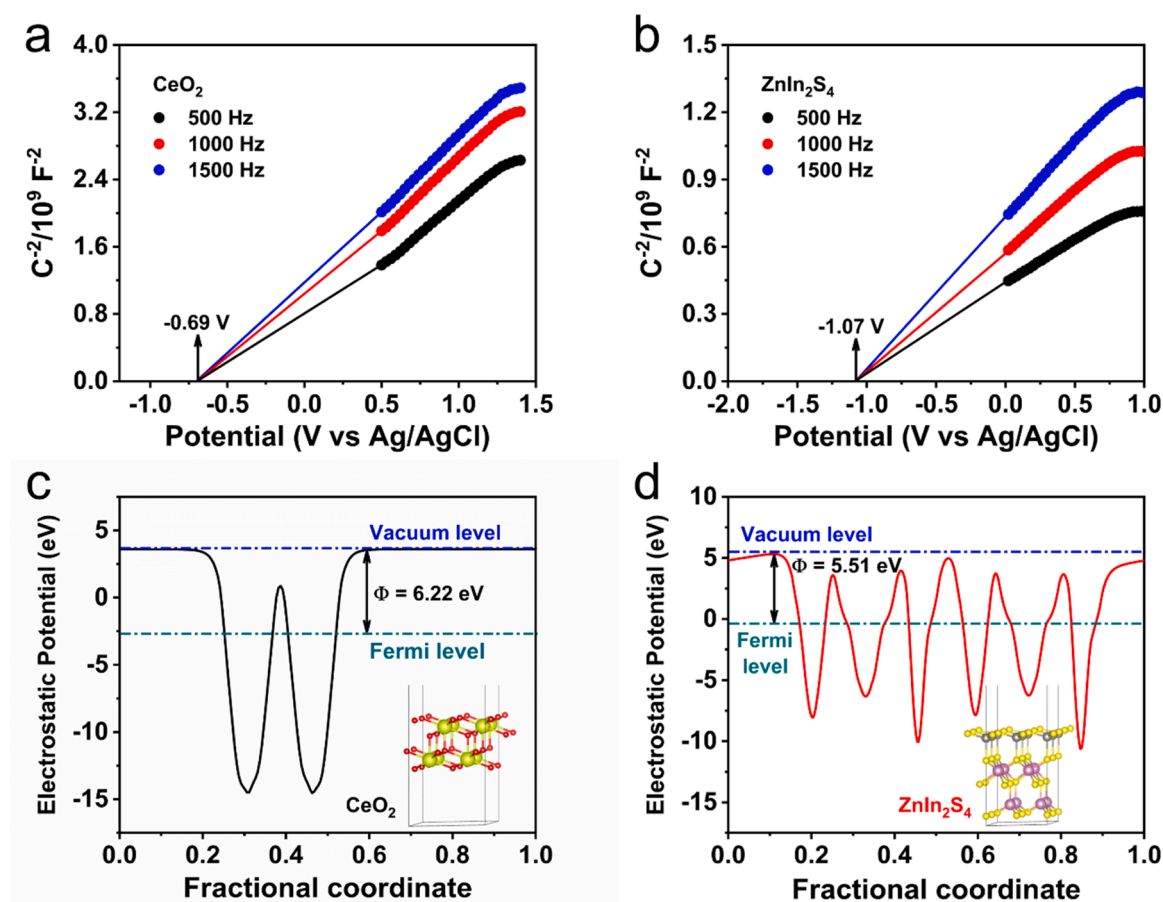
**Fig. 6.** (a, b) Mott–Schottky plots of $CeO_2$ and $ZnIn_2S_4$. (c, d) Calculated electrostatic potentials of $CeO_2$ and $ZnIn_2S_4$, where the insets are the structural models of $CeO_2$ and $ZnIn_2S_4$, respectively.
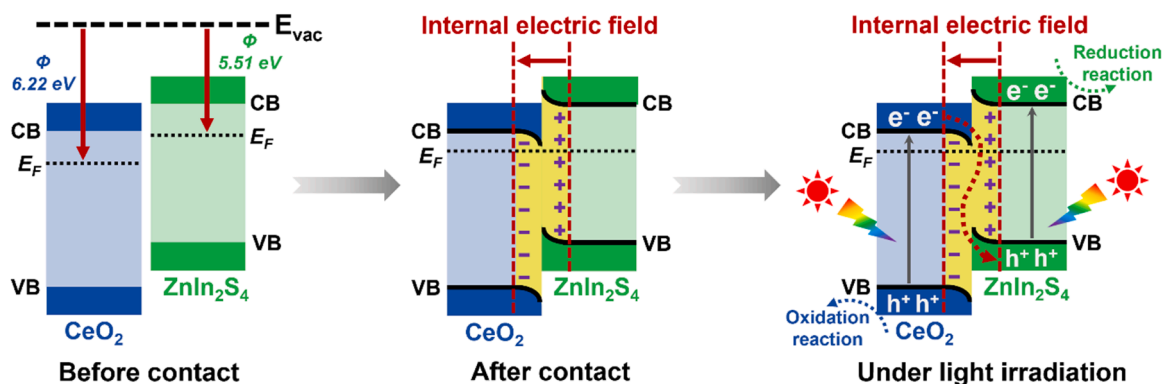


**Fig. 7.** The formation of the S-scheme $ZnIn_2S_4/CeO_2$ heterojunction photocatalyst and the proposed charge transfer mechanism.

contact and light exposure, which well agrees with the S-scheme mechanism [16–18,61].

To reveal the S-scheme mechanism over the $ZnIn_2S_4/CeO_2$ heterojunction photocatalyst, the band structures of $CeO_2$ and $ZnIn_2S_4$ are further measured. The conduction band (CB) potentials of $CeO_2$ and $ZnIn_2S_4$ were determined based on the Mott–Schottky (M–S) plots at various frequencies. As displayed in Fig. 6a,b, both $CeO_2$ and $ZnIn_2S_4$ are n-type semiconductors because of the positive slopes [46,55], and their corresponding flat-band potentials ($E_{fb}$) are $-0.69$ and $-1.07$ V (vs Ag/AgCl, pH 7), respectively. The CB potentials of $CeO_2$ and $ZnIn_2S_4$ are then estimated to be $-0.49$ and $-0.87$ V (vs NHE, pH 7), respectively. Given their band gap values (Fig. 2d), the valence band (VB)

potentials of $CeO_2$ and $ZnIn_2S_4$ are calculated as 2.37 and 1.76 V (vs NHE, pH 7) (Fig. S17) according to $E_{VB} = E_{CB} + E_g$, respectively. The work function ($\Phi$) is an important parameter to demonstrate the interface charge transfer in the heterojunction photocatalysts [59,62,63]. Fig. 6c,d exhibit that the $\Phi$ values calculated via density functional theory (DFT) for $CeO_2$ and $ZnIn_2S_4$ were 6.22 eV and 5.51 eV, respectively. The relationship between the vacuum level ($E_{vac}$) and Fermi level ($E_F$) is expressed as following formula: $\Phi = E_{vac} - E_F$, where $E_{vac}$ is assumed as 0 eV. As a result, the $E_F$ of $CeO_2$ and $ZnIn_2S_4$ are determined as $-6.22$ and $-5.51$ eV, respectively.

Subsequently, based on the aforementioned results of XPS, work function and Fermi level, the S-scheme charge transfer mechanism for
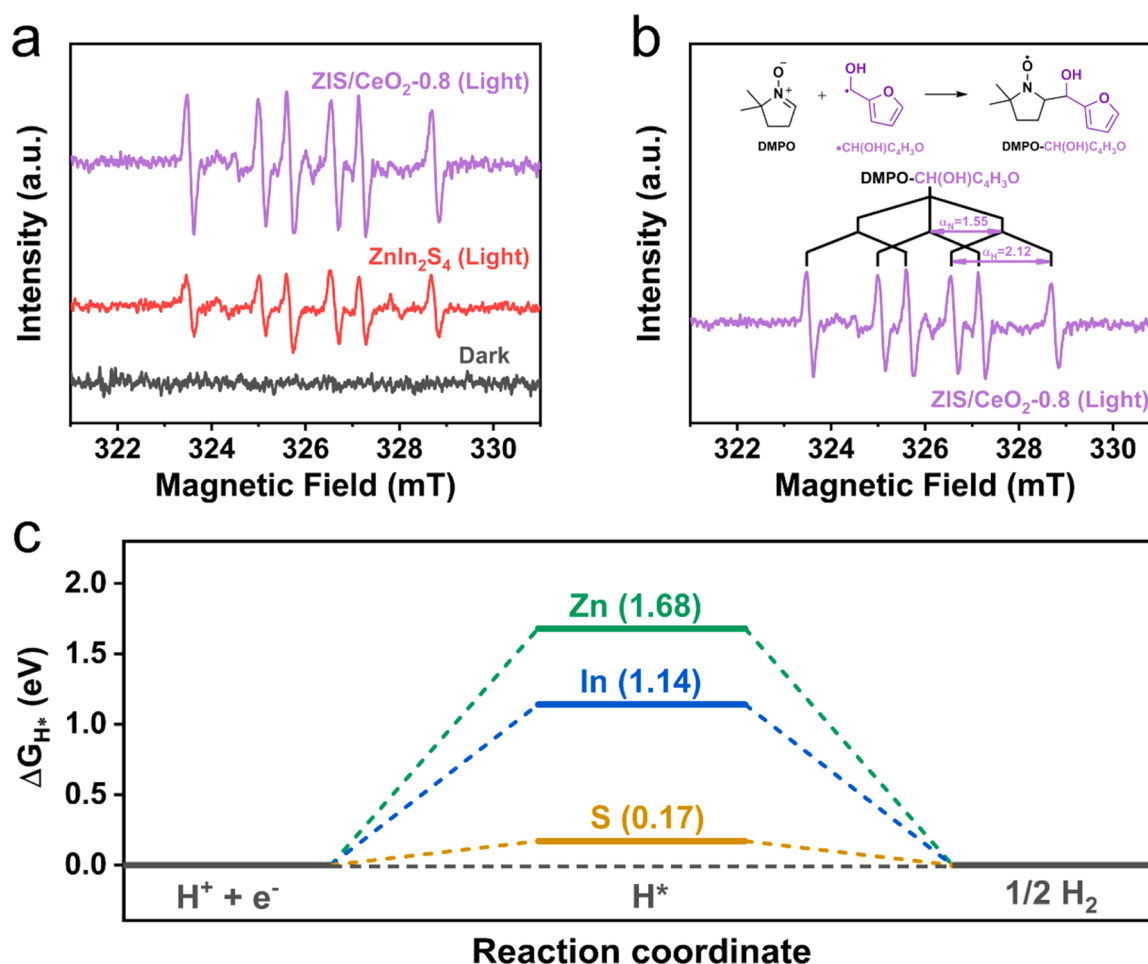
**Fig. 8.** (a) ESR spectra of the formed·CH(OH)C$_4$H$_3$O carbon-centered radicals over ZnIn$_2$S$_4$ and ZIS/CeO$_2$-0.8 photocatalysts in FOL aqueous solution. (b) The quantitative analysis result of ESR spectrum of ZIS/CeO$_2$-0.8 heterojunctions with visible light irradiation.

the ZnIn$_2$S$_4$/CeO$_2$ heterojunction is proposed. As shown in Fig. 7, CeO$_2$ has a larger (lower) work function (Fermi level) than that of ZnIn$_2$S$_4$. When CeO$_2$ and ZnIn$_2$S$_4$ are come into close contact, the electrons in ZnIn$_2$S$_4$ are spontaneously migrated to CeO$_2$ for reaching Fermi level equilibrium. Obviously, ZnIn$_2$S$_4$ loses electrons and is positively charged at the interface, whereas CeO$_2$ is negatively charged at the interface due to the accumulation of electrons. This electron flow process induces the formation of an internal electric field directed from ZnIn$_2$S$_4$ to CeO$_2$ and bends their energy band edges at the interface. Under light irradiation, the electrons in both ZnIn$_2$S$_4$ and CeO$_2$ are stimulated from VBs to CBs. Driven by the formed internal electric field and bent energy bands, the photogenerated electrons in the CeO$_2$ CB are easily transferred to the VB of ZnIn$_2$S$_4$ and recombine with photogenerated holes there. Finally, the powerful photogenerated electrons and holes are preserved in the CB of ZnIn$_2$S$_4$ and VB of CeO$_2$, respectively, for the photocatalytic redox reaction. Therefore, this S-scheme transfer path not only effectively promotes the spatial separation of photogenerated carriers, but also maximizes the redox capacity of the heterojunction photocatalyst.

To give more evidence of the strong reductive electrons and oxidative holes in the S-scheme ZnIn$_2$S$_4$/CeO$_2$ heterojunction, electron spin resonance (ESR) spectroscopy was performed as shown in Figs. S18 and S19. No ESR signal is detected in the blank (without photocatalyst) experiments when using 5,5-dimethyl-1-pyrroline N-oxide (DMPO) as a spin-trapping agent, indicating that DMPO molecule has no paramagnetic center [61]. Fig. S18 depicts the pure ZnIn$_2$S$_4$ has a stronger DMPO-O$_2^-$ signal than that of CeO$_2$, because the CB potential in ZnIn$_2$S$_4$ is more negative than that of CeO$_2$. Besides, the DMPO-·O$_2^-$ signal comes

from the reduction of O$_2$, and ESR signal of DMPO-·O$_2^-$ in the ZIS/CeO$_2$-0.8 heterojunctions is much higher than single component, which is ascribed to the suppressed recombination and higher utility of the electrons having strong O$_2$ reduction ability. As shown in Fig. S19, owing to the considerable recombination of electron-hole pairs in bare CeO$_2$, the ZnIn$_2$S$_4$ also exhibits a slightly stronger DMPO-·OH signal than CeO$_2$. Similarly, the signal intensity of DMPO-·OH for ZIS/CeO$_2$-0.8 heterojunctions is higher relative to that of CeO$_2$ and ZnIn$_2$S$_4$, implying that the photogenerated holes with powerful oxidation capability are reserved in the VB of CeO$_2$ upon unique S-scheme heterojunction construction.

Meanwhile, for the purpose of deeply investigating the information of reactive intermediates in the photocatalytic redox reaction, the ESR characterization was also used to monitor radical intermediates on ZnIn$_2$S$_4$ and ZnIn$_2$S$_4$/CeO$_2$-0.8 heterojunctions. As shown in Fig. 8a, six characteristic signal peaks are obviously observed in both samples under visible light irradiation. Besides, the measured α$_N$ = 1.55 and α$_H$ = 2.12 correspond to the nitrogen hyperfine splitting and hydrogen hyperfine splitting for the nitroxide nitrogen [64–66], respectively (Fig. 8b), which belong to DMPO-CH(OH)C$_4$H$_3$O [49,64]. This result indicates the holes in ZIS/CeO$_2$-0.8 heterojunctions are favorable for dehydrogenation process of the α-C-H bond during the photocatalytic oxidation of FOL reaction [65]. Notably, the characteristic signal peak intensity of ZIS/CeO$_2$-0.8 heterojunctions is much stronger than that of pure ZnIn$_2$S$_4$ under the same conditions, which indicates that the higher concentration and stronger oxidation capability of the photogenerated holes over the S-scheme ZnIn$_2$S$_4$/CeO$_2$ heterojunction photocatalyst can promote
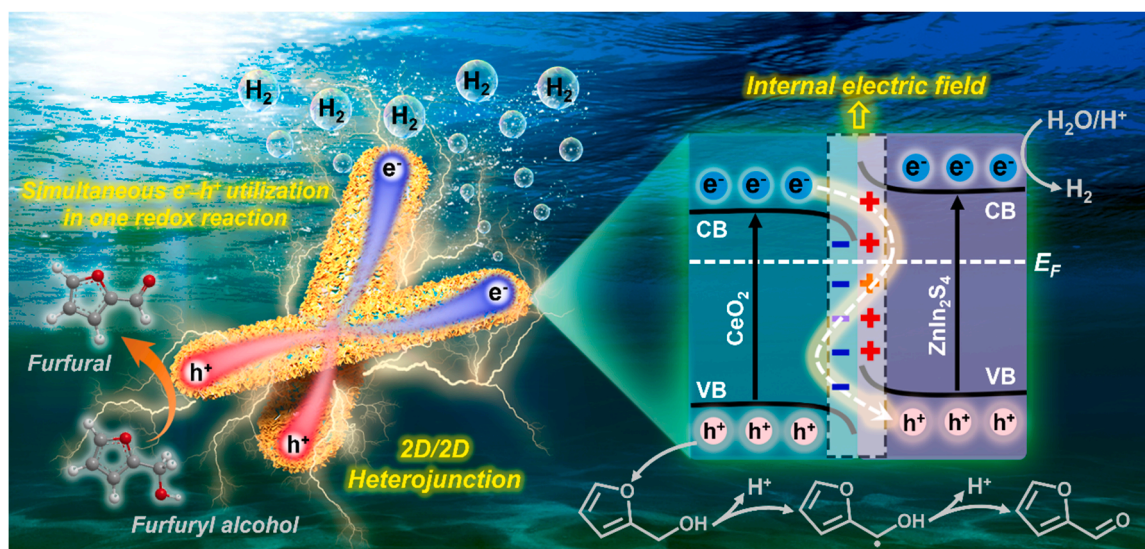
**Fig. 9.** A reasonable catalytic mechanism for cooperative photoredox reaction containing $H_2$ production and FOL conversion over 2D/2D $ZnIn_2S_4/CeO_2$ heterojunction.

the generation of more reactive intermediates, thus contributing to the improvement of photocatalytic performance.

Furthermore, the Gibbs free energy of hydrogen adsorption ($\Delta G_{H*}$) is an important parameter of the activity for photocatalytic $H_2$ production reaction. It is well known that the closer the $\Delta G_{H*}$ approximates to zero, the higher the activity [7,67,68]. Fig. S20 shows the optimized structural models of the $ZnIn_2S_4/CeO_2$ heterojunction with hydrogen adsorption on different active sites, and corresponding calculation results are displayed in free energy diagram (Fig. 8c). Evidently, $\Delta G_{H*} = 0.17$ eV for the S sites, which is much smaller than those of Zn and In sites, indicating the S sites are the active sites for $H_2$ production.

Based on all the above results, a reasonable photocatalytic enhancement mechanism of $H_2$ production coupled with FOL oxidation conversion on the 2D/2D $ZnIn_2S_4/CeO_2$ heterojunction is proposed (Fig. 9). When $ZnIn_2S_4$ nanosheets are tightly anchored on $CeO_2$ nanosheets, a robust internal electric field is constructed at the contact interface. Under visible light irradiation, the electrons are first excited from their VB to CB in $CeO_2$ and $ZnIn_2S_4$. Then, the internal electric field induces the photogenerated electrons of $CeO_2$ to recombine with holes of $ZnIn_2S_4$ through S-scheme charge transfer pathway, which allows the electrons and holes with higher redox powers to be spatially separated. Furthermore, the 2D/2D heterointerfaces can provide abundant and shortest channels for accelerated charge transfer, thus also playing a positive role in inhibiting electron-hole recombination. Finally, the accumulated photogenerated electrons on the CB of $ZnIn_2S_4$ combine with surface-adsorbed protons to catalytically produce $H_2$. Concurrently, the preserving holes in the VB of $CeO_2$ undergo an activation process of α-C-H bond of FOL, generating·$CH(OH)C_4H_3O$ carbon radicals and protons, and the powerful holes further oxidize these radicals to obtain FAL products. Therefore, thanks to the synergistic effect of the strong internal electric field and 2D/2D intimate interface, the photogenerated electrons and holes are separated and transferred more efficiently, the photocatalytic redox performance is remarkably enhanced.

## 4. Conclusion

In summary, a 2D/2D S-scheme $ZnIn_2S_4/CeO_2$ heterojunction photocatalyst was successfully prepared for cooperative $H_2$ production and FOL oxidation. The small $ZnIn_2S_4$ nanosheets were immobilized on larger $CeO_2$ nanosheets, resulting in abundant 2D/2D heterointerfaces, which is beneficial for providing the broad and short charge transfer paths. Compared with pure $CeO_2$ and $ZnIn_2S_4$, the optimized $ZnIn_2S_4/$ $CeO_2$ heterojunction photocatalyst exhibits much greater bifunctional photocatalytic performance, with the $H_2$ production rate of 1.34 mmol $g^{-1}$ $h^{-1}$ and FAL generation rate of 1.24 mmol $g^{-1}$ $h^{-1}$, as well as good photochemical stability. The detailed experimental characterization analyses and DFT calculations unveil that the improved redox performance is attributed to the highly efficient separation and migration of photogenerated carriers with forceful redox abilities in the S-scheme heterojunction system. This work supplies a reference on the design and construction of efficient, stable and bifunctional heterojunction photocatalysts for the collaborative reactions of $H_2$ production and alcohol conversion.

## CRediT authorship contribution statement

**Guping Zhang:** Investigation, Data validation, Writing – original draft. **Shuting Huang & Xunxun Li:** Investigation, Data curation. **Dongyun Chen:** Supervision, Writing – review & editing, Funding acquisition. **Najun Li, Qingfeng Xu & Hua Li:** Writing – review & editing. **Jianmei Lu:** Supervision, Funding acquisition, Project administration.

## Declaration of Competing Interest

The authors declare that they have no known competing financial interests or personal relationships that could have appeared to influence the work reported in this paper.

## Data Availability

Data will be made available on request.

## Acknowledgements

# Appendix A. Supporting information

Supplementary data associated with this article can be found in the online version at doi:10.1016/j.apcatb.2023.122725.

# References

[1] Q. Zhu, Q. Xu, M. Du, X. Zeng, G. Zhong, B. Qiu, J. Zhang, Recent progress of metal sulfide photocatalysts for solar energy conversion, Adv. Mater. 34 (2022) 2202929.

[2] E. Nikoloudakis, I. López-Duarte, G. Charalambidis, K. Ladomenou, M. Ince, A. G. Coutsolelos, Porphyrins and phthalocyanines as biomimetic tools for photocatalytic H$_2$ production and CO$_2$ reduction, Chem. Soc. Rev. 51 (2022) 6965–7045.

[3] X. Li, Z. Wang, L. Wang, Metal–organic framework-based materials for solar water splitting, Small Sci. 1 (2021) 2000074.

[4] J. Zhang, W. Hu, S. Cao, L. Piao, Recent progress for hydrogen production by photocatalytic natural or simulated seawater splitting, Nano Res. 13 (2020) 2313–2322.

[5] Q. Zhu, Z. Xu, B. Qiu, M. Xing, J. Zhang, Emerging cocatalysts on g-C$_3$N$_4$ for photocatalytic hydrogen evolution, Small 17 (2021) 2101070.

[6] X. Wang, X. Wang, J. Huang, S. Li, A. Meng, Z. Li, Interfacial chemical bond and internal electric field modulated Z-scheme S$_v$-ZnIn$_2$S$_4$/MoSe$_2$ photocatalyst for efficient hydrogen evolution, Nat. Commun. 12 (2021) 4112.

[7] S. Cao, J. Yu, S. Wageh, A.A. Al-Ghamdi, M. Mousavi, J.B. Ghasemi, F. Xu, H$_2$-production and electron-transfer mechanism of a noble-metal-free WO$_3$@ZnIn$_2$S$_4$ S-scheme heterojunction photocatalyst, J. Mater. Chem. A 10 (2022) 17174–17184.

[8] V.B.-Y. Oh, S.-F. Ng, W.-J. Ong, Shining light on ZnIn$_2$S$_4$ photocatalysts: promotional effects of surface and heterostructure engineering toward artificial photosynthesis, EcoMat 4 (2022), e12204.

[9] Y. Ren, J.J. Foo, D. Zeng, W.-J. Ong, ZnIn$_2$S$_4$-based nanostructures in artificial photosynthesis: insights into photocatalytic reduction toward sustainable energy production, Small Struct. 3 (2022) 2200017.

[10] C. Liu, Q. Zhang, Z. Zou, Recent advances in designing ZnIn$_2$S$_4$-based heterostructured photocatalysts for hydrogen evolution, J. Mater. Sci. Technol. 139 (2023) 167–188.

[11] G. Zhang, H. Wu, D. Chen, N. Li, Q. Xu, H. Li, J. He, J. Lu, A mini-review on ZnIn$_2$S$_4$-Based photocatalysts for energy and environmental application, Green Energy Environ. 7 (2022) 176–204.

[12] R. Yang, L. Mei, Y. Fan, Q. Zhang, R. Zhu, R. Amal, Z. Yin, Z. Zeng, ZnIn$_2$S$_4$-based photocatalysts for energy and environmental applications, Small Methods 5 (2021) 2100887.

[13] T. Su, C. Men, L. Chen, B. Chu, X. Luo, H. Ji, J. Chen, Z. Qin, Sulfur vacancy and Ti$_3$C$_2$T$_x$ cocatalyst synergistically boosting interfacial charge transfer in 2D/2D Ti$_3$C$_2$T$_x$/ZnIn$_2$S$_4$ heterostructure for enhanced photocatalytic hydrogen evolution, Adv. Sci. 9 (2022) 2103715.

[14] Y. Chao, P. Zhou, J. Lai, W. Zhang, H. Yang, S. Lu, H. Chen, K. Yin, M. Li, L. Tao, C. Shang, M. Tong, S. Guo, Ni$_{1-x}$Co$_x$Se$_2$−C/ZnIn$_2$S$_4$ hybrid nanocages with strong 2D/2D hetero-interface interaction enable efficient H$_2$-releasing photocatalysis, Adv. Funct. Mater. 31 (2021) 2100923.

[15] G. Zuo, Y. Wang, W.L. Teo, A. Xie, Y. Guo, Y. Dai, W. Zhou, D. Jana, Q. Xian, W. Dong, Y. Zhao, Ultrathin ZnIn$_2$S$_4$ nanosheets anchored on Ti$_3$C$_2$T$_x$ MXene for photocatalytic H$_2$ evolution, Angew. Chem. Int. Ed. 59 (2020) 11287–11292.

[16] Q. Xu, L. Zhang, B. Cheng, J. Fan, J. Yu, S-scheme heterojunction photocatalyst, Chem 6 (2020) 1543–1559.

[17] L. Zhang, J. Zhang, H. Yu, J. Yu, Emerging S-scheme photocatalyst, Adv. Mater. 34 (2022) 2107668.

[18] L. Wang, B. Zhu, J. Zhang, J.B. Ghasemi, M. Mousavi, J. Yu, S-scheme heterojunction photocatalysts for CO$_2$ reduction, Matter 5 (2022) 4187–4211.

[19] Q. Li, L. Song, Z. Liang, M. Sun, T. Wu, B. Huang, F. Luo, Y. Du, C.-H. Yan, A review on Ceo$_2$-based electrocatalyst and photocatalyst in energy conversion, Adv. Energy Sustain. Res 2 (2021) 2000063.

[20] D.P.H. Tran, M.-T. Pham, X.-T. Bui, Y.-F. Wang, S.-J. You, CeO$_2$ as a photocatalytic material for CO$_2$ conversion: A review, Sol. Energy 240 (2022) 443–466.

[21] Q. Zhou, L. Zhang, L. Zhang, B. Jiang, Y. Sun, In-situ constructed 2D/2D ZnIn$_2$S$_4$/ Bi$_4$Ti$_3$O$_{12}$ S-scheme heterojunction for degradation of tetracycline: Performance and mechanism insights, J. Hazard. Mater. 438 (2022), 129438.

[22] X. Dang, M. Xie, F. Dai, J. Guo, J. Liu, X. Lu, Ultrathin 2D/2D ZnIn$_2$S$_4$/g-C$_3$N$_4$ nanosheet heterojunction with atomic-level intimate interface for photocatalytic hydrogen evolution under visible light, Adv. Mater. Interfaces 8 (2021) 2100151.

[23] Y. Qin, H. Li, J. Lu, Y. Feng, F. Meng, C. Ma, Y. Yan, M. Meng, Synergy between van der waals heterojunction and vacancy in ZnIn$_2$S$_4$/g-C$_3$N$_4$ 2D/2D photocatalysts for enhanced photocatalytic hydrogen evolution, Appl. Catal. B: Environ. 277 (2020), 119254.

[24] J. Ran, H. Zhang, J. Qu, J. Shan, K. Davey, J.M. Cairney, L. Jing, S.-Z. Qiao, Significantly Raised Visible-Light Photocatalytic H$_2$ Evolution on a 2D/2D ReS$_2$/ In$_2$ZnS$_4$ van der Waals Heterostructure, Small 17 (2021) 2100296.

[25] J. Xu, W. Zhong, D. Gao, X. Wang, P. Wang, H. Yu, Phosphorus-enriched platinum diphosphide nanodots as a highly efficient cocatalyst for photocatalytic H$_2$ evolution of CdS, Chem. Eng. J. 439 (2022), 135758.

[26] J. Bai, R. Shen, W. Chen, J. Xie, P. Zhang, Z. Jiang, X. Li, Enhanced photocatalytic H$_2$ evolution based on a Ti$_3$C$_2$/Zn$_{0.7}$Cd$_{0.3}$S/Fe$_2$O$_3$ Ohmic/S-scheme hybrid heterojunction with cascade 2D coupling interfaces, Chem. Eng. J. 429 (2022), 132587.

[27] R. Shen, L. Zhang, N. Li, Z. Lou, T. Ma, P. Zhang, Y. Li, X. Li, W.–N. Bonds, Precisely boost Z-scheme interfacial charge transfer in g-C$_3$N$_4$/WO$_3$ heterojunctions for enhanced photocatalytic H$_2$ evolution, ACS Catal. 12 (2022) 9994–10003.

[28] X. Jing, N. Lu, J. Huang, P. Zhang, Z. Zhang, One-step hydrothermal synthesis of S-defect-controlled ZnIn$_2$S$_4$ microflowers with improved kinetics process of charge-carriers for photocatalytic H$_2$ evolution, J. Energy Chem. 58 (2021) 397–407.

[29] M. Gao, F. Tian, X. Zhang, Y. Liu, Z. Chen, Y. Yu, W. Yang, Y. Hou, Fast charge separation and transfer strategy in polymeric carbon nitride for efficient photocatalytic H$_2$ evolution: Coupling surface Schottky junctions and interlayer charge transfer channels, Nano Energy 103 (2022), 107767.

[30] M. Dai, Z. He, P. Zhang, X. Li, S. Wang, ZnWO$_4$-ZnIn$_2$S$_4$ S-scheme heterojunction for enhanced photocatalytic H$_2$ evolution, J. Mater. Sci. Technol. 122 (2022) 231–242.

[31] M.-Y. Qi, M. Conte, M. Anpo, Z.-R. Tang, Y.-J. Xu, Cooperative coupling of oxidative organic synthesis and hydrogen production over semiconductor-based photocatalysts, Chem. Rev. 121 (2021) 13051–13085.

[32] B. Xia, Y. Zhang, B. Shi, J. Ran, K. Davey, S.-Z. Qiao, Photocatalysts for hydrogen evolution coupled with production of value-added chemicals, Small Methods 4 (2020) 2000063.

[33] K. Jing, W. Ma, Y. Ren, J. Xiong, B. Guo, Y. Song, S. Liang, L. Wu, Hierarchical Bi$_2$MoO$_6$ spheres in situ assembled by monolayer nanosheets toward photocatalytic selective oxidation of benzyl alcohol, Appl. Catal. B: Environ. 243 (2019) 10–18.

[34] J. Zou, Z. Wang, W. Guo, B. Guo, Y. Yu, L. Wu, Photocatalytic selective oxidation of benzyl alcohol over ZnTi-LDH: the effect of surface OH groups, Appl. Catal. B: Environ. 260 (2020), 118185.

[35] Y. Zhang, S.-J. Park, Phosphorization-derived MoP@MoO$_{3-x}$ nanowires for selective photocatalytic oxidation of benzyl alcohol to benzaldehyde, J. Catal. 394 (2021) 332–341.

[36] H. Wang, Y. Song, J. Xiong, J. Bi, L. Li, Y. Yu, S. Liang, L. Wu, Highly selective oxidation of furfuryl alcohol over monolayer titanate nanosheet under visible light irradiation, Appl. Catal. B: Environ. 224 (2018) 394–403.

[37] J. Wang, X. Liu, Z. Li, Acceptorless photocatalytic dehydrogenation of furfuryl alcohol (FOL) to Furfural (FAL) and Furoic Acid (FA) over Ti$_3$C$_2$T$_x$/CdS under Visible Light, Chem. Asian J. 16 (2021) 2932–2938.

[38] G. Zhao, S.A. Bonke, S. Schmidt, Z. Wang, B. Hu, T. Falk, Y. Hu, T. Rath, W. Xia, B. Peng, A. Schnegg, Y. Weng, M. Muhler, Highly efficient and selective aerobic oxidation of cinnamyl alcohol under visible light over Pt-loaded NaNbO$_3$ enriched with oxygen vacancies by Ni doping, ACS Sustain. Chem. Eng. 9 (2021) 5422–5429.

[39] R. Mariscal, P. Maireles-Torres, M. Ojeda, I. Sádaba, M. López Granados, Furfural: a renewable and versatile platform molecule for the synthesis of chemicals and fuels, Energy Environ. Sci. 9 (2016) 1144–1189.

[40] C. Xu, E. Paone, D. Rodríguez-Padrón, R. Luque, F. Mauriello, Recent catalytic routes for the preparation and the upgrading of biomass derived furfural and 5-hydroxymethylfurfural, Chem. Soc. Rev. 49 (2020) 4273–4306.

[41] Z. Wang, L. Wang, B. Cheng, H. Yu, J. Yu, Photocatalytic H$_2$ evolution coupled with furfuralcohol oxidation over Pt-modified ZnCdS solid solution, Small Methods 5 (2021) 2100979.

[42] Q. Dai, Z. Zhang, J. Yan, J. Wu, G. Johnson, W. Sun, X. Wang, S. Zhang, W. Zhan, Phosphate-functionalized CeO$_2$ nanosheets for efficient catalytic oxidation of dichloromethane, Environ. Sci. Technol. 52 (2018) 13430–13437.

[43] G. Zhang, D. Chen, N. Li, Q. Xu, H. Li, J. He, J. Lu, Construction of hierarchical hollow Co$_9$S$_8$/ZnIn$_2$S$_4$ tubular heterostructures for highly efficient solar energy conversion and environmental remediation, Angew. Chem. Int. Ed. 59 (2020) 8255–8261.

[44] G. Zhang, J. Sun, D. Chen, N. Li, Q. Xu, H. Li, J. He, J. Lu, Hierarchical core–shell heterostructures of ZnIn$_2$S$_4$ nanosheets on electrospun In$_2$O$_3$ nanofibers with highly enhanced photocatalytic activity, J. Hazard. Mater. 398 (2020), 122889.

[45] H. Yan, R. Wang, R. Liu, T. Xu, J. Sun, L. Liu, J. Wang, Recyclable and reusable direct Z-scheme heterojunction CeO$_2$/TiO$_2$ nanotube arrays for photocatalytic water disinfection, Appl. Catal. B: Environ. 291 (2021), 120096.

[46] J. Hu, T. Yang, J. Chen, X. Yang, J. Qu, Y. Cai, Efficient solar-driven H$_2$O$_2$ synthesis in-*situ* activation to purify water via cascade reaction on ZnIn$_2$S$_4$-based heterojunction, Chem. Eng. J. 430 (2022), 133039.

[47] W. Zhu, S. Xiao, D. Zhang, P. Liu, H. Zhou, W. Dai, F. Liu, H. Li, Highly efficient and stable Au/CeO$_2$–TiO$_2$ photocatalyst for nitric oxide abatement: potential application in flue gas treatment, Langmuir 31 (2015) 10822–10830.

[48] Y. Sun, X. Yuan, Y. Wang, W. Zhang, Y. Li, Z. Zhang, J. Su, J. Zhang, S. Hu, CeO$_2$ quantum dots anchored g-C$_3$N$_4$: synthesis, characterization and photocatalytic performance, Appl. Surf. Sci. 576 (2022) 151901.

[49] C.-L. Tan, M.-Y. Qi, Z.-R. Tang, Y.-J. Xu, Cocatalyst decorated ZnIn$_2$S$_4$ composites for cooperative alcohol conversion and H$_2$ evolution, Appl. Catal. B: Environ. 298 (2021) 120541.

[50] J. Zhang, L. Zheng, F. Wang, C. Chen, H. Wu, S.A.K. Leghari, M. Long, The critical role of furfural alcohol in photocatalytic H$_2$O$_2$ production on TiO$_2$, Appl. Catal. B: Environ. 269 (2020) 118770.

[51] S. Wang, B.Y. Guan, X. Wang, X.W.D. Lou, Formation of hierarchical Co$_9$S$_8$@ ZnIn$_2$S$_4$ heterostructured cages as an efficient photocatalyst for hydrogen evolution, J. Am. Chem. Soc. 140 (2018) 15145–15148.

[52] X. Peng, L. Ye, Y. Ding, L. Yi, C. Zhang, Z. Wen, Nanohybrid photocatalysts with ZnIn$_2$S$_4$ nanosheets encapsulated UiO-66 octahedral nanoparticles for visible-light-driven hydrogen generation, Appl. Catal. B: Environ. 260 (2020) 118152.

[53] S. Wang, B.Y. Guan, X.W.D. Lou, Construction of ZnIn$_2$S$_4$–In$_2$O$_3$ hierarchical tubular heterostructures for efficient CO$_2$ photoreduction, J. Am. Chem. Soc. 140 (2018) 5037–5040.

[54] Q. Mu, Y. Su, Z. Wei, H. Sun, Y. Lian, Y. Dong, P. Qi, Z. Deng, Y. Peng, Dissecting the interfaces of MOF-coated CdS on synergized charge transfer for enhanced photocatalytic $CO_2$ reduction, J. Catal. 397 (2021) 128–136.

[55] L. Zhu, H. Li, P. Xia, Z. Liu, D. Xiong, Hierarchical ZnO decorated with $CeO_2$ nanoparticles as the direct Z-scheme heterojunction for enhanced photocatalytic activity, ACS Appl. Mater. Interfaces 10 (2018) 39679–39687.

[56] Y. Wang, X. Hao, L. Zhang, Y. Li, Z. Jin, Rational design of all-solid-state 0D/2D $Mn_{0.2}Cd_{0.8}S/CeO_2$ direct Z-scheme for photocatalytic hydrogen evolution, Energy Fuels 34 (2020) 2599–2611.

[57] S. Zhang, J. Guo, W. Zhang, H. Gao, J. Huang, G. Chen, X. Xu, Dopant and defect doubly modified $CeO_2/g-C_3N_4$ nanosheets as 0D/2D Z-scheme heterojunctions for photocatalytic hydrogen evolution: experimental and density functional theory studies, ACS Sustain. Chem. Eng. 9 (2021) 11479–11492.

[58] Y. Shao, J. Hu, T. Yang, X. Yang, J. Qu, Q. Xu, C.M. Li, Significantly enhanced photocatalytic in-*situ* $H_2O_2$ production and consumption activities for efficient sterilization by $ZnIn_2S_4/g-C_3N_4$ heterojunction, Carbon 190 (2022) 337–347.

[59] L. Wang, B. Cheng, L. Zhang, J. Yu, In situ irradiated XPS investigation on S-scheme $TiO_2@ZnIn_2S_4$ photocatalyst for efficient photocatalytic $CO_2$ reduction, Small 17 (2021) 2103447.

[60] J. Li, C. Wu, J. Li, B. Dong, L. Zhao, S. Wang, 1D/2D $TiO_2/ZnIn_2S_4$ S-scheme heterojunction photocatalyst for efficient hydrogen evolution, Chin. J. Catal. 43 (2022) 339–349.

[61] P. Xia, S. Cao, B. Zhu, M. Liu, M. Shi, J. Yu, Y. Zhang, Designing a 0D/2D S-scheme heterojunction over polymeric carbon nitride for visible-light photocatalytic inactivation of bacteria, Angew. Chem. Int. Ed. 59 (2020) 5218–5225.

[62] F. Xu, K. Meng, B. Cheng, S. Wang, J. Xu, J. Yu, Unique S-scheme heterojunctions in self-assembled $TiO_2/CsPbBr_3$ hybrids for $CO_2$ photoreduction, Nat. Commun. 11 (2020) 4613.

[63] M. Tan, Y. Ma, C. Yu, Q. Luan, J. Li, C. Liu, W. Dong, Y. Su, L. Qiao, L. Gao, Q. Lu, Y. Bai, Boosting photocatalytic hydrogen production via interfacial engineering on 2D ultrathin Z-scheme $ZnIn_2S_4/g-C_3N_4$ heterojunction, Adv. Funct. Mater. 32 (2022) 2111740.

[64] J. Hu, X. Li, J. Qu, X. Yang, Y. Cai, T. Yang, F. Yang, C.M. Li, Bifunctional honeycomb hierarchical structured 3D/3D $ReS_2/ZnIn_2S_4-S_v$ heterojunction for efficient photocatalytic $H_2$-evolution integrated with biomass oxidation, Chem. Eng. J. 453 (2023), 139957.

[65] J. Wan, L. Liu, Y. Wu, J. Song, J. Liu, R. Song, J. Low, X. Chen, J. Wang, F. Fu, Y. Xiong, Exploring the Polarization Photocatalysis of $ZnIn_2S_4$ Material toward Hydrogen Evolution by Integrating Cascade Electric Fields with Hole Transfer Vehicle, Adv. Funct. Mater. 32 (2022) 2203252.

[66] Y.-H. Li, M.-Y. Qi, Z.-R. Tang, Y.-J. Xu, Coupling Organic Synthesis and Hydrogen Evolution over Composite $WO_3/ZnIn_2S_4$ Z-Scheme Photocatalyst, J. Phys. Chem. C. 126 (2022) 1872–1880.

[67] T. Wang, X. Tao, X. Li, K. Zhang, S. Liu, B. Li, Synergistic Pd Single Atoms, Clusters, and Oxygen Vacancies on $TiO_2$ for Photocatalytic Hydrogen Evolution Coupled with Selective Organic Oxidation, Small 17 (2021) 2006255.

[68] S. Shen, Z. Lin, K. Song, Z. Wang, L. Huang, L. Yan, F. Meng, Q. Zhang, L. Gu, W. Zhong, Reversed Active Sites Boost the Intrinsic Activity of Graphene-like Cobalt Selenide for Hydrogen Evolution, Angew. Chem. Int. Ed. 60 (2021) 12360–12365.